Nanoscale

PAPER

View Article Online
View Journal | View Issue

Cite this: *Nanoscale*, 2024, **16**, 1291

Probing spin waves in Co_3O_4 nanoparticles for magnonics applications†

Mikhail Feygenson, *[a,b,c] Zhongyuan Huang,‡[d] Yinguo Xiao, [d] Xiaowei Teng, [e] Wiebke Lohstroh,[f] Nileena Nandakumaran,[g] Jörg C. Neuefeind,[h] Michelle Everett,[h] Andrey A. Podlesnyak, [h] Germán Salazar-Alvarez, [c] Seda Ulusoy,[c] Mario Valvo, [i] Yixi Su,[j] Sascha Ehlert,[b] Asma Qdemat,[g] Marina Ganeva, [j] Lihua Zhang[k] and Meigan C. Aronson[l]

Received 2nd September 2023,
Accepted 13th November 2023

DOI: 10.1039/d3nr04424f

rsc.li/nanoscale

The magnetic properties of spinel nanoparticles can be controlled by synthesizing particles of a specific shape and size. The synthesized nanorods, nanodots and cubic nanoparticles have different crystal planes selectively exposed on the surface. The surface effects on the static magnetic properties are well documented, while their influence on spin waves dispersion is still being debated. Our ability to manipulate spin waves using surface and defect engineering in magnetic nanoparticles is the key to designing magnonic devices. We synthesized cubic and spherical nanoparticles of a classical antiferromagnetic material Co_3O_4 to study the shape and size effects on their static and dynamic magnetic proprieties. Using a combination of experimental methods, we probed the magnetic and crystal structures of our samples and directly measured spin wave dispersions using inelastic neutron scattering. We found a weak, but unquestionable, increase in exchange interactions for the cubic nanoparticles as compared to spherical nanoparticle and bulk powder reference samples. Interestingly, the exchange interactions in spherical nanoparticles have bulk-like properties, despite a ferromagnetic contribution from canted surface spins.

1 Introduction

The magnetic nanomaterials offer a unique opportunity to broaden our understanding of fundamental exchange interactions inside a solid-state matter on an atomic scale that underlines its macroscopic properties. The interactions are tailored by virtue of the finite-size effects resulting from a large fraction of the surface atoms. It is possible to further affect exchange interactions in nanoparticles by deliberately changing their shape to expose selected crystal planes. The nanoparticles of different shapes retain their chemical composition, in contrast to the bulk materials, in which the exchange interactions can only be altered by an isotope substitution, application of high pressure and extreme magnetic fields.

Here, we present a comprehensive study of the dynamic magnetic properties of the spherical and cubic Co_3O_4 nanoparticles using a combination of advanced neutron scattering methods. The bulk Co_3O_4 crystallizes in a normal spinel structure and it becomes antiferromagnetic below the Néel temperature (T_N) of about 40 K.[1] The origin of the antiferromagnetic (AFM) ordering in Co_3O_4 is ascribed to the exchange interactions between magnetic Co^{2+} ions *via* non-magnetic intervening O^{2-} ion.[1–3] The strength of the interactions is defined by the exchange constants J_1 and J_2, corresponding to the AFM interactions between the nearest Co^{2+} ions and weak ferro-

---

[a] European Spallation Source ERIC, SE-221 00 Lund, Sweden. E-mail: mikhail.feygenson@ess.eu
[b] Jülich Centre for Neutron Science (JCNS-1) at Forschungszentrum Jülich, D-52425 Jülich, Germany
[c] Department of Materials Science and Engineering, Uppsala University, Box 35, 751 03 Uppsala, Sweden
[d] School of Advanced Materials, Peking University, Shenzhen Graduate School, Shenzhen 518055, China
[e] Worcester Polytechnic Institute, Department of Chemical Engineering, Worcester 01609, USA
[f] Heinz Maier-Leibnitz Zentrum (MLZ), Technische Universität München, Lichtenbergstr. 1, 8574 Garching, Germany
[g] Jülich Centre for Neutron Science (JCNS-2) and Peter Grünberg Institute (PGI-4), Jülich GmbH, 52425 Jülich, Germany
[h] Neutron Scattering Division, Oak Ridge National Laboratory, Oak Ridge, Tennessee 37831, USA
[i] Department of Chemistry, Uppsala University, 75121 Uppsala, Sweden
[j] Jülich Centre for Neutron Science (JCNS-4) at Heinz Maier-Leibnitz-Zentrum (MLZ), Forschungszentrum Jülich GmbH, Lichtenbergstr. 1, 85747 Garching, Germany
[k] Center for Functional Nanomaterials, Brookhaven National Laboratory, Upton, New York 11973-5000, USA
[l] Stewart Blusson Quantum Matter Institute, University of British Columbia, Vancouver, BC V6T 1Z4, Canada

† Electronic supplementary information (ESI) available. See DOI: **https://doi.org/10.1039/d3nr04424f**

‡ This author contributed equally to this work.

magnetic (FM) interactions between the next-nearest Co^{2+} ions. The strength of AFM interactions depends on Co–O bond lengths, the titling angle between them, and occupancies of the atoms within the exchange path.[4] Although the earliest study of the origin of the antiferromagnetic order in the bulk powder of Co_3O_4 dates back to 1964,[1] the interest in the Co_3O_4 nanoparticles was recently revived by advances in shape and surface engineering that resulted in the synthesis of nanocubes, nanorods, nanoplates, nanotubes and 3D-nanonet hollow structures of Co_3O_4.[5–16] These nanostructured Co_3O_4 materials have shown particular characteristics and superior performance in a variety of applications, including thermoelectric power generation, advanced supercapacitors, quantum tunneling, phonon transmission and lithium storage capacity.[15,17–19]

The AFM ordering of the Co_3O_4 makes it also possible to use the Co_3O_4 nanoparticles in magnonics applications. In this revolutionary concept, spin waves or magnons are used to carry information.[20–23] The manipulation of the spin waves is a cornerstone of magnonics applications, that was successfully achieved in thin films and millimeter-sized ferrimagnetic crystal.[24–26] The spin wave detection in magnetic nanoparticles is the next step in the same direction, aiming to miniaturize magnonic devices by bringing them to the nanoscale. The AFM nanoparticles are particularly attractive for applications due to the higher energy required for switching between different magnetic states and hence operating into the THz range.[27–29] However, the finite-size and shape effects on the spin wave properties are needed to be understood first. In the particular case of the Co_3O_4 nanoparticles, a direct impact of surface engineering on exchange interactions has been demonstrated.[30,31] The Co_3O_4 nanoparticles with exposed (100) and (111) crystal planes showed an induced magnetic moment on nominally non-magnetic Co^{3+} ions, while for (110) planes, Co^{3+} ions remain non-magnetic.

We used inelastic neutron scattering to experimentally study spin waves dispersions and to directly measure J_1 and J_2 exchange constants in spherical and cubic Co_3O_4 nanoparticles, as well as in their bulk powder counterpart. The inelastic neutron scattering measurements were successfully used in the past to detect the spin waves in a variety of magnetic nanoparticles.[32–34] We also revised the experimental J_1 value for the bulk Co_3O_4 powder, in order to provide an additional input for density functional theory calculations, that currently estimate values of J_1 varied by an order of magnitude.[35,36]

2 Experimental

We synthesized cubic Co_3O_4 nanoparticles using Co nanoparticles prepared by the thermal decomposition of $Co_2(CO)_8$ in hot oleic acid as described in.[37,38] Once the particles have fully formed, we annealed them at 400 °C for 4 hours inside a vacuum furnace. The use of the annealing temperature above the boiling point of the oleic acid (360 °C) ensured the absence of the surfactant coating of the cubic nanoparticles. The spherical Co_3O_4 nanoparticles and reference bulk powder of Co_3O_4 were purchased from Sigma-Aldrich.

TEM measurements were carried out in the Ernst Ruska-Centre at Forschungszentrum Jülich with a Philips CM20 TEM and FEITecnai G2 F20 using an accelerating voltage of 200 kV. The SEM studies were performed using a Hitachi SU8000 instrument at an electron acceleration voltage of 20 kV. Additional HRTEM measurements were performed at Uppsala University. The samples were dispersed in toluene and drop-casted on 400 mesh carbon-coated copper grids. The particles were investigated using a FEI Titan Themis microscope with a Schottky field-emission gun operating at an accelerating voltage of 200 kV. The images were acquired using a BM-Ceta Camera.

The DC magnetization measurements were carried out using a Quantum Design Magnetic Property Measurement System (MPMS). For the measurements, 10 μL of the original aliquots were dispersed in 50 μL of liquid paraffin and then injected into a standard gelatin capsule to reduce inter-particle interactions. The gelatin capsules were fastened in plastic straws for immersion into the magnetometer. In order to measure the exchange bias field, a sample is cooled from 300 K to 5 K in an applied magnetic field of 70 kOe. The magnetization is then measured as a function of an applied magnetic field. The exchange bias field is calculated as $H_{EB} = |H_{c1} + H_{c2}|/2$, where H_{c1} and H_{c2} are the negative and positive coercive fields, respectively. The standard field-cooled (FC) and zero-field-cooled (ZFC) measurements of temperature-dependent magnetization were used to determine T_N. FC and ZFC measurements were carried out in the field of 500 Oe.

The time-of-flight (TOF) neutron diffraction experiments were performed on the Nanoscale-Ordered Materials Diffractometer (NOMAD) at Spallation Neutron Source (SNS) at Oak Ridge National Laboratory.[39] The low-temperature measurements were done using an Orange-type cryostat. NOMAD detectors were calibrated using scattering from diamond powder. The magnetic structure refinements of the data were done using Jana2006 software,[40] which was adopted for handling neutron TOF diffraction data from six detector banks. In order to obtain the structural factor $S(Q)$ the scattering intensity was normalized to the scattering from a solid vanadium rod and the background was subtracted. The pair-distribution function (PDF) was obtained by the Fourier transform of $S(Q)$ at $Q_{min} = 0.08$ Å^{-1} and $Q_{max} = 31.5$ Å^{-1}:

$$G(r) = \frac{2}{\pi}\int_{Q_{min}}^{Q_{max}} Q(S(Q) - 1)\sin(Qr)\mathrm{d}Q \tag{1}$$

We used the Cold Neutron Chopper Spectrometer (CNCS) at the SNS at Oak Ridge National Laboratory[41] to perform zero field TOF inelastic neutron scattering experiments on nanoparticle powders with the incident wavelength of $\lambda_i = 2.34$ Å ($E_i = 15$ meV). Additional temperature-dependent inelastic neutron scattering measurements were carried out at TOFTOF instrument at Heinz Maier-Leibnitz Zentrum. Two incident wavelengths $\lambda_{i,1} = 2$ Å ($E_{i,1} = 9$ meV) and $\lambda_{i,2} = 5$ Å ($E_{i,2} = 3.3$ meV) were used for accessing the medium and high energy resolutions, respectively. The empty sample container and vanadium solid rod were measured with both instruments. The vanadium measurements were used to define the resolution function of each instrument. The CNCS data have provided access to the energy gain and the energy loss parts of excitations (Fig. S5†), while only the energy gain part of the TOFTOF data was analyzed. The TOFTOF data were reduced using Mantid software.[42]

Room temperature Raman measurements were conducted at Uppsala University using a Renishaw (inVia) spectrometer with a built-in optical microscope (Leica) and by employing two different excitation wavelengths of 532 and 785 nm, respectively. The latter were provided by different solid-state laser diodes. Prior to the analyses, the spectrometer was calibrated using a Si wafer to obtain a characteristic reference peak at ~520 cm^{-1}. A low laser power was utilized for the respective measurements and the laser beam was focused onto the surface of the various samples *via* a 50× lens.

3 Results and discussion

Three samples were investigated in our work: spherical Co_3O_4 nanoparticles, cubic Co_3O_4 nanoparticles and reference bulk powder. The properties of all samples are summarized in Table 1.

3.1 Structural characterization

A combination of transmission electron microscopy (TEM) and scanning electron microscopy (SEM) measurements was used to characterize the overall size, shape, and crystallinity of our samples. Representative TEM and SEM images are shown in Fig. 1. The cubic sample shows polydisperse nanoparticles. The majority of the nanoparticles are best described by a rectangular shape with clear-cut edges (Fig. 1a). The spherical nanoparticles appear to be globular with a high degree of agglomeration (Fig. 1b). The spherical nanoparticles appeared to be amorphous, but high-resolution TEM (Fig. 1b, inset) and X-ray powder diffraction studies (Fig. S1†) confirmed their crystallinity. The bulk sample shows polyhedron crystallites as large as several micrometers in size (Fig. 1c).

3.2 Magnetization measurements

The ZFC and FC magnetizations of the cubic and spherical nanoparticles peak at T_N ~45 K (Fig. 1d and e). At temperatures above T_N, the long-range AFM order is lost and nanoparticles are transitioned into the paramagnetic phase. In this phase, the temperature dependence of the ZFC and FC magne-

Table 1 Properties of Co_3O_4 nanoparticles obtained from refinements of neutron scattering data. Here, *d* is the crystallite size, T_N is the Néel temperature, *m* is the magnetic moment per Co^{2+} at 10 K and *a* is the lattice constant at the same temperature. J_1 and J_2 are refined exchange constants for the nearest-neighbors AFM and next nearest-neighbors FM interactions, respectively. D_S is the uniaxial single-ion anisotropy constant

Sample	d (nm)	T_N (K)	a (Å)	m (μ_B)	J_1 (meV)	J_2 (meV)	D_S (meV)
Sphere	33(3)	30.1(2)	8.075(2)	2.76(2)	−7.60	1.10	0.0154
Cubic	61(2)	32.2(1)	8.086(3)	2.88(2)	−7.72	1.10	0.0154
Bulk	2500(1)	42.4(8)	8.086(3)	3.01(2)	−7.60	1.10	0.0154

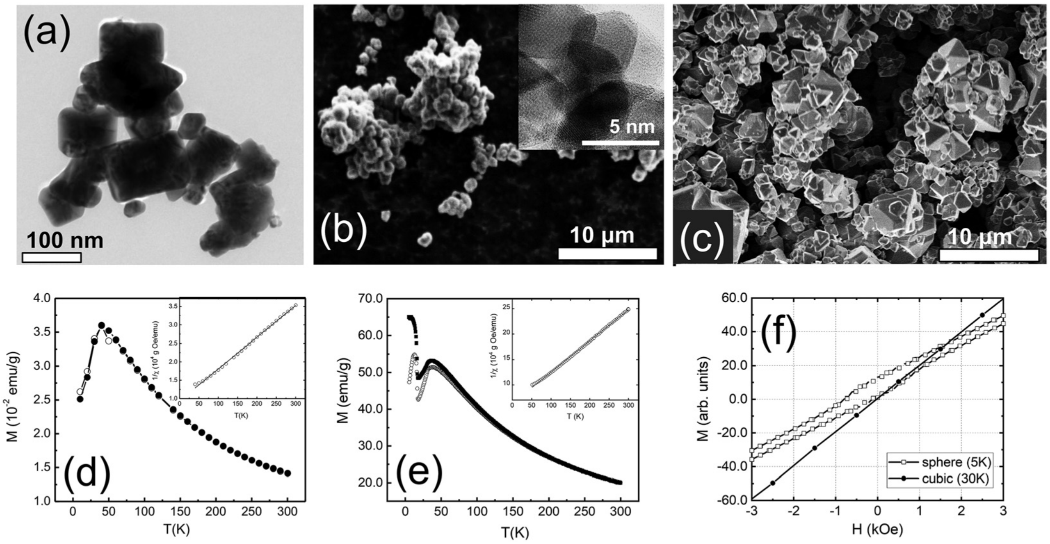

Fig. 1 Representative TEM and SEM images of (a) cubic, (b) spherical and (c) bulk Co_3O_4 samples. The temperature-dependent ZFC (open symbols) and FC (filled symbols) magnetizations for (d) cubic and (e) spherical nanoparticles. Insets show inverse susceptibility χ as a function of temperature (open symbols) with the fit to Curie-Weiss law (solid line). (f) Field-dependent DC magnetizations of spherical and cubic Co_3O_4 nanoparticles, measured at 5 K and 30 K, respectively.

tizations is well described by the Curie–Weiss law. The strength of AFM interactions can be estimated by fitting magnetic susceptibility χ to the modified Curie–Weiss equation ($\chi = \chi_0 + [C/(T + \theta)]$) well above T_N. The fits are shown in the insets of Fig. 1d and e for cubic and spherical nanoparticles. In the case of cubic nanoparticles, we derived $C = 1.16 \times 10^{-2}$ emu K g^{-1} Oe, $\theta = 109$ K and $\chi_0 = 1.06 \times 10^{-4}$ emu g^{-1} Oe, in good agreement with the previous reports for the bulk Co_3O_4.[43,44] For spherical nanoparticles we obtained $C = 1.63 \times 10^{-2}$ emu K g^{-1} Oe, $\theta = 103$ K and $\chi_0 = 1.57 \times 10^{-5}$ emu g^{-1} Oe. The negative sign of θ suggests dominating AFM interactions for all samples. The strength of the interactions is rather similar because values of θ for nanoparticles are close 110 K, previously reported for the bulk Co_3O_4.[16,45]

The magnetic properties of cubic and spherical nanoparticles are distinctively different at low temperatures. ZFC magnetization of the spherical nanoparticles peaks at ~25 K, while FC magnetization gradually increases and saturates below 25 K. Other researchers have observed similar DC magnetization dependence in Co_3O_4 nanoparticles, attributed to the coexistence of AFM-ordered core and FM-like surface shell of uncompensated spins with a freezing temperature of 25 K.[46–48] The alternative explanation of this transition is a spin glass-like phase of the surface magnetic moments.[49,50] However, we found no signatures of the spin-glass phase below 25 K in our neutron diffraction and inelastic neutron scattering data,[51] at least within the experimental uncertainty. The existence of an FM-like surface shell is further confirmed by the observation of an exchange bias field (H_{EB}) below 25 K. The maximum field $H_{EB} = 357(8)$ Oe was obtained at 5 K after cooling in 70 kOe field from the room temperature (Fig. 1f). The presence of the exchange bias effect is a clear indication of the coupling between the AFM core and the FM-like surface shell, previously documented in the literature for Co_3O_4 nanoparticles.[52–57] In the case of cubic nanoparticles, no exchange bias was observed under similar experimental conditions.

3.3 Raman scattering

We examine the structural properties of our samples with Raman scattering measurements at two wavelengths of 532 and 785 nm. A comparison of the normalized spectra for both nanoparticles and the bulk reference powder is presented in Fig. 2a and b, while their respective as-recorded spectral signals are shown in Fig. S2.† All the samples exhibit five Raman-active modes confirming the formation of the pure cubic phase of Co_3O_4 with a normal spinel structure.[58–60] The peaks for all samples are centered at around similar positions: 197 cm^{-1} (F_{2g}), 483 cm^{-1} (E_g), 523 cm^{-1} (F_{2g}), 621 cm^{-1} (F_{2g}), and 692 cm^{-1} (A_{1g}) as shown in Fig. 2a and b. The position of each peak is ascribed to a characteristic vibration mode (see ESI†).

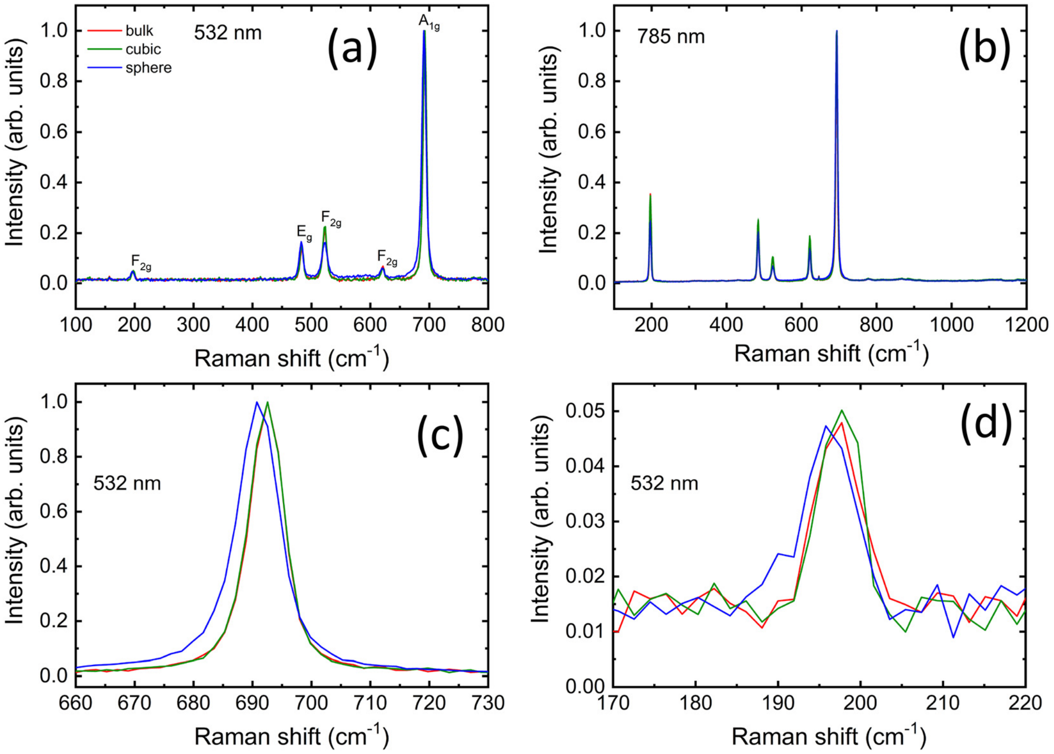

Fig. 2 Comparison of normalized Raman spectra for all three samples obtained using different excitation wavelengths of (a) 532 nm and (b) 785 nm. Expanded views of the spectra in (a) show a slight red-shift and broadening of the most intense A_{1g} peak at high wavenumbers (c), and similarly of the weakest F_{2g} mode at low wavenumbers (d). Note also a decrease of the relative intensities of the peaks in (b) only for the spherical nanoparticles.

All normalized Raman spectra look very similar and spherical nanoparticles are the only sample that displays a slight redshift of ~2 cm^{-1} for the A_{1g} mode when measured with a 532 nm wavelength (Fig. 2c). Moreover, the spherical nanoparticles show a moderate broadening of all the peaks compared to those displayed by the other two samples (Table S1†). The peak broadening is less visible in the spectra recorded with 785 nm excitation wavelength (Table S2†) and no shift is detected for any peak position in this case, while the intensities of the remaining modes appear more pronounced. The most likely explanation for both phenomena is a higher degree of a structural disorder in spherical nanoparticles, previously suggested for the similar Co_3O_4 nanostructures.[59,61,62]

Interestingly, the slight red shift in Fig. 2c, d and Fig. S2a† affects only the A_{1g} mode at ~690 cm^{-1} and the F_{2g} vibration at ~196 cm^{-1}, whereas the positions of the other peaks are not influenced. If it were an optical phonon confinement effect,[63,64] the peak positions of the five active modes would sensibly be shifted toward lower wavenumbers, while this is not the case. Pronounced agglomeration for the spherical nanoparticles (see also Fig. 1b), due to their larger surface-to-volume ratio compared to the other samples, could influence their thermal response,[18] especially under conditions of elevated light absorption, *e.g.* during resonant Raman scattering (RRS). RRS causes excitation of electronic levels and substantial enhancement of some vibrational modes. Under such conditions and high absorption, the light penetration is typically limited to a few tens of nanometers,[64] thereby making this analysis more surface sensitive. Using 532 nm instead of 785 nm should in principle allow a shallower penetration depth ($\delta_p = \lambda_{exc}/4\pi nk$) and thus probe more effectively the particle surface *via* RRS.[64] Considering the reduced number of counts compared to the as-recorded spectra obtained with the 785 nm laser (see Fig. S2a and b†) and the negligible influence of thermal effects due to the purposeful use of low laser power, the results in Fig. 2a and Fig. S2a† suggest that surface defects, local lattice distortions and disorder represent the main cause for the slight changes in the spectral features of the spherical nanoparticles under RRS at 532 nm. In fact, the peaks remained sharp and hardly shifted to lower wavenumbers, while the peak broadening for the spherical nanoparticles appeared moderate, especially when compared to those reported for agglomerated Co_3O_4 nanoparticles measured with similar laser power, whose spectral features sensibly red-shifted and exhibited much broader lines.[18,65] Therefore, this confirms that the surface properties of the spherical nanoparticles differ from those of the cubic nanoparticles and bulk powder.

3.4 Neutron diffraction studies

We combined neutron powder diffraction and pair-distribution function (PDF) measurements, to unambiguously determine our samples' crystal and magnetic structures. The quality of Rietveld refinements of the neutron diffraction data is demonstrated in Fig. 3a and b. The refined average crystal structure is cubic for all samples with the space group $Fd\bar{3}m$.[66] It is a normal spinel with the Co^{2+} and Co^{3+} ions occupying tetrahedral and octahedral sites, respectively. While positions of structural peaks are the same for all samples, the peak width of nanoscaled samples is broader as compared to the bulk counterpart due to the finite particle size. The crystalline sizes equal to 33(3) and 61(2) nm for spherical and cubic nanoparticles, respectively were derived from the Rietveld refinements (Tables S3 and S4†). The most intriguing conclusion of the average crystal structure study is a difference in lattice constant values between the three samples shown in Fig. 3c. The lattice constant of cubic nanoparticles is higher than the bulk sample, while the lattice constant of spherical nanoparticles is smaller.

The magnetic structure of our samples was refined from neutron diffraction data collected below T_N. In agreement with previous neutron diffraction studies of Co_3O_4 powders,[1,46,67] we found that the magnetic structure is best described by a propagation vector $k = (0, 0, 0)$, *i.e.* the magnetic unit cell is identical to the nuclear one. The two primary peaks below T_N can be indexed to the (111) and (200) peaks of the bulk Co_3O_4 structure. The first peak at $Q_{111} = 1.33$ Å^{-1} constitutes structural and magnetic contributions, while the second peak $Q_{200} = 1.56$ Å^{-1} is purely magnetic. Additional diffuse scattering had to be added in the modeling of the intensity of Q_{111} peak for all three samples (see Fig. S3†). This magnetic diffuse scattering was previously observed with neutron diffraction studies of the bulk Co_3O_4. It corresponds to the disordered short-range magnetic state resembling spiral spin liquid. The correlation length of the disordered state was estimated using the Scherrer formula[68] $\zeta = d_{111}^2/\Delta d_{111}$, where d_{111} is the position and Δd_{111} is the full width at half-maximum of the Q_{111} peak. We found ζ equal to 9.8(2) nm, 6.7(3) nm and 12.4(1) nm, for the spherical, cubic and bulk samples. The correlation length in spherical nanoparticles is about 30% of their crystalline size, implying a non-negligible role of this magnetically disordered phase in their magnetic properties.

In our model, only Co^{2+} ions bear magnetic moments. The magnetic moment of spherical nanoparticles is reduced down to $2.76(2)\mu_B$ from the value of $3.01(2)\mu_B$ observed for the bulk and cubic nanoparticles at 10 K. We found no deviation from a cubic symmetry in the crystal structural or additional magnetic phase transitions below T_N in both of our nanoparticle samples. We obtained T_N for each sample from mean-field fits of the magnetic moment temperature dependence (Fig. 3d). T_N is decreasing from its bulk value of 42.4(8) K with the particle size down to 32.2(1) K and 30.1(2) K, for cubic and spherical particles, respectively. The result agrees well with the finite-size effects reduction of T_N previously reported for Co_3O_4 nanoparticles.[45,47,69,70]

We further investigate the local crystal structure of our samples using neutron PDF measurements. The purpose of PDF studies was to verify any deviations from the average crystal structure derived from Rietveld refinements. Nanoparticles are prone to dislocations, stress, vacancies and anti-phase boundaries, which all can influence local crystal structure and consequently, the strength of the AFM

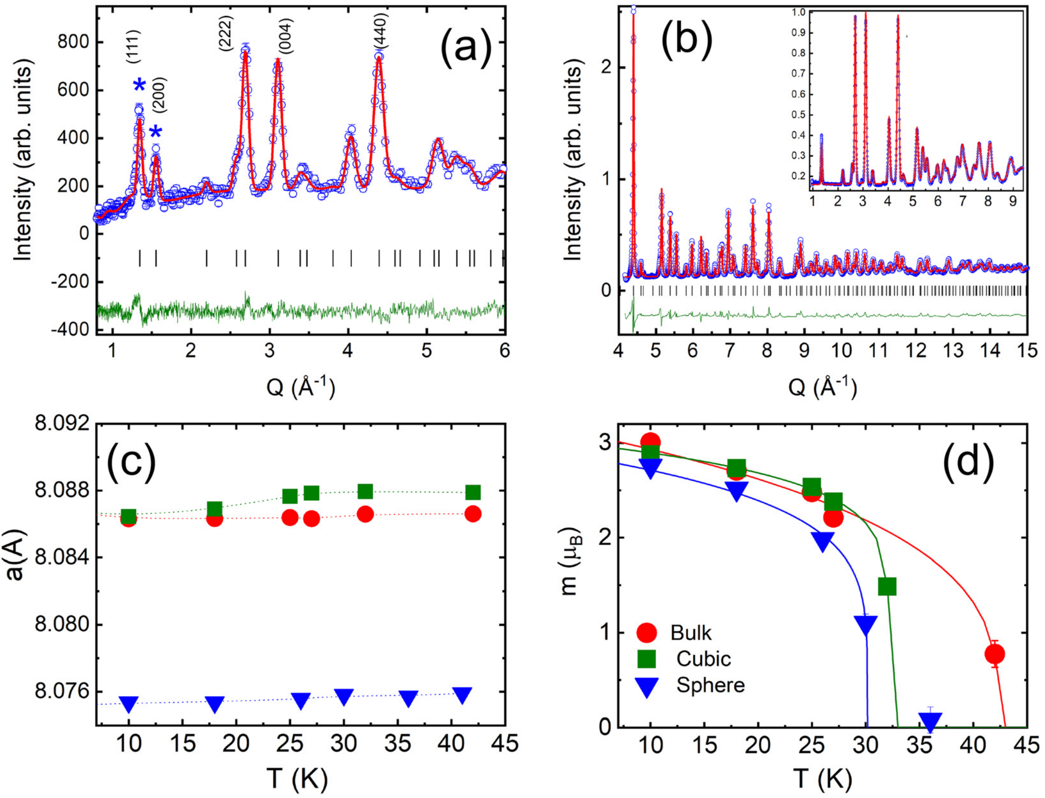

Fig. 3 NOMAD TOF diffraction data for cubic Co_3O_4 nanoparticles from the forward scattering bank at 10 K (a) and the backscattering bank at 100 K (b), with experimental data as blue open circles, the calculated pattern in red, and the difference curve in green. Inset shows an expanded view of the same data, with no indications of magnetic Bragg peaks. Temperature dependencies of the lattice constant (c) and the magnetic moment per Co^{2+} (d) for the spherical, cubic and bulk samples. Solid lines are mean-field fits with T_N listed in Table 1.

interactions.[71,72] Most recent examples include modification of the local structure of iron oxide nanoparticles due to vacancies and non-stoichiometry.[73,74] Specifically for Co_3O_4 samples, we used PDF measurements to investigate local structural transitions, which were suggested as one of the reasons for the incommensurate AFM order observed with muon spin rotation and relaxation method in bulk Co_3O_4.[43]

Neutron PDF data for all three samples are qualitatively similar. We fitted neutron PDF data using the average crystal structure obtained with the Rietveld refinements as a starting model (Fig. 4a). The PDF analysis indicated no deviations of the local structure from the cubic symmetry or any signs of inverse spinel structure for both nanoparticle samples. The lattice constants obtained from the refinement of the PDF data are consistent with Rietveld refinement results (Fig. S4a†). The spherical nanoparticles have the smallest lattice constant. The most significant difference between the samples is observed for the spherical nanoparticles between 3.0 and 3.7 Å at 10 K. The intensities of the three peaks at 3.15, 3.35 and 3.57 AA are reduced (Fig. 4b). The position of the first peak at 3.15 Å

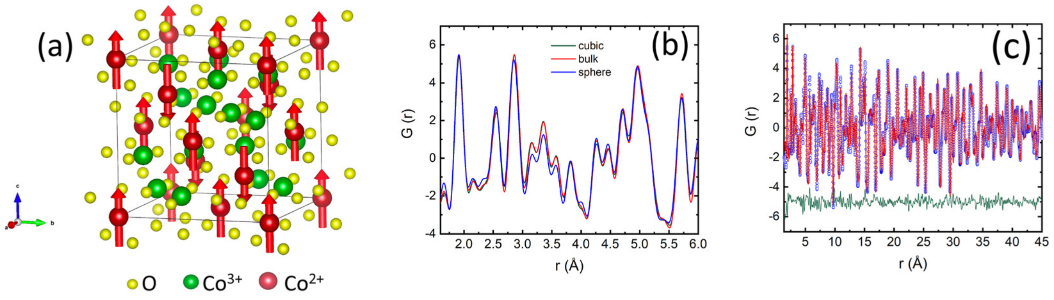

Fig. 4 (a) Magnetic and crystal structure of the bulk Co_3O_4 obtained with Rietveld refinements. (b) Comparison of the experimental neutron PDF for all three samples at 10 K. (c) Analysis of the PDF data of cubic nanoparticles at 10 K with experimental data in open circles, calculated pattern in red, and difference curve in green.

corresponds to an O–O atomic pair. The second peak is a superposition of Co–Co and Co–O atomic pairs, while the last peak corresponds to Co–O pair (Fig. S4b†). The reduction of intensity in PDF peaks compared to the bulk indicates that the atoms in corresponding pairs have a lower coordination number. We refined the occupancies of O and Co atoms while modeling the neutron PDF data (Table S4†). The results of the PDF data refinements for cubic nanoparticles are shown in Fig. 4c and for the bulk in Fig. S4c.† We found that occupancies of O and Co atoms are reduced for the spherical nanoparticles, as compared to the bulk and cubic nanoparticles (Table S3†). Neutron diffraction is not sensitive to the valence state of Co atoms, however previous density function theory (DFT) calculations confirmed that the formation of the Co^{2+} defects is more likely than the formation of Co^{3+} defects, because of the lower formation energy of Co^{2+} vacancies.[59]

3.5 Inelastic neutron scattering measurements

The spin wave properties of our samples were studied with TOF inelastic neutron scattering measurements (INS). We found no previous reports on TOF INS of polycrystalline a powder or single crystal of Co_3O_4. Growing a single crystal of Co_3O_4 is extremely challenging. The main issue is the decomposition of Co_3O_4 at 900 °C which limits applications of conventional crystal growth methods. The Co_3O_4 is carcinogenic and extraordinary safety measures have to be taken in order to handle it at elevated temperatures.[75]

The overview of INS data is shown in Fig. 5. The energy and wave-vector dependence of the scattered intensity $I(Q,E)$ is plotted for T = 5 K for the cubic nanoparticles and bulk powder (Fig. 5a and b). Similar for all three samples, the inelastic excitation peaked near 6 meV, and shows dispersion over the entire Q-range with its intensity decreasing strongly with increased wave vector Q. The dispersion is periodic and matches perfectly the periodicity of the Bravais magnetic lattice derived from the magnetic structure (Fig. S6 and S7†). The excitations are only observed below T_N for each individual sample. Since the excitation signals in the spectrum possess a characteristic dispersion in the low-energy regions and the scattering intensity decreases with increasing Q following the magnetic form factor, it is fair to conclude that the signals are contributions from magnetic spin waves. Similar spin wave dispersions for the nanoparticle and bulk samples confirm that they are inherently specific to the magnetic properties of Co_3O_4. We found no evidence of finite-size induced phonon dispersions nor excitations associated with the collective nanoparticle modes, at least within our experimental energy window of 15 meV. Fig. 5c and d show the energy E dependence of the scattered intensity $I(E)$ for the cubic nanoparticles and bulk powder, integrated over wave vectors Q, for temperatures above and below T_N. Above T_N, the scattering is quasielastic (QE) for both samples. As the temperature is reduced, the QE linewidth is reduced and the overall scattering intensity decreases. QE scattering collapses below T_N, for both samples and the inelastic peak begins to emerge. It changes its position and becomes more intense as the temperature further decreases. At the lowest temperature of 5 K, the peak position for the cubic nanoparticles is slightly but visibly increased to E = 6.2 meV, compared to the value of 6.0 meV for both bulk powder and spherical nanoparticles.

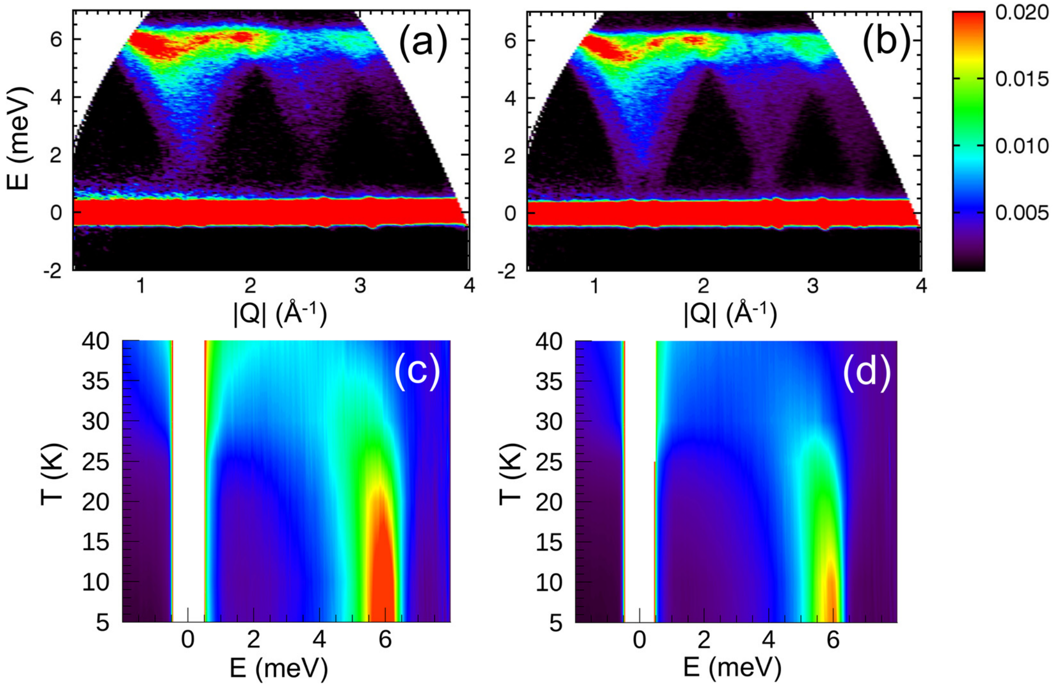

Fig. 5 The scattered intensity $I(Q,E)$ at 5 K for (a) cubic nanoparticles and (b) bulk powder. The Q-integrated scattered intensity $I(E)$ at different temperatures for (c) cubic nanoparticles and (d) bulk powder.

The neutron diffraction studies of our samples showed a relatively large magnetic moment of Co^{2+} ions, therefore the spin wave dispersion can be analyzed by the Heisenberg model with a spin Hamiltonian:

$$H = -\frac{1}{2}\sum_{i,j} J_{ij} S_i \cdot S_j - D_S \sum_i S_{i,z}^2 \tag{2}$$

where, S_i is the spin operator for the ith site, J_{ij} denotes the exchange constants, and D_S is the uniaxial single-ion anisotropy constant. According to eqn (2), a positive J_{ij} corresponds to a FM interaction and a negative J_{ij} corresponds to an AFM interaction, while a positive D_S of a certain magnitude corresponds to the formation of an anisotropy-induced energy gap in the spin wave spectrum. In our analysis, only two exchange constants were used: J_1 to describe the nearest-neighbor interactions and J_2 to describe the next nearest-neighbor interactions between Co^{2+} ions. The bosonic Hamiltonian in the momentum space was obtained by applying the Holstein–Primakoff transformation for spin operators. The Hamiltonian was diagonalized numerically to calculate the eigenvalues related to the spin wave dispersion and eigenvectors associated with a spin wave structure factor (see ESI†). The following neutron cross-section was used to model the experimental INS data:

$$\frac{d^2\sigma}{d\Omega dE} = \frac{k_f}{k_i}\left(\frac{1}{2}\gamma r_0 g F(Q)\right)^2 e^{-2W} \times \sum_{\alpha,\beta}\left(\delta_{\alpha,\beta} - {}_{\alpha}\,{}_{\beta}\right) S^{\alpha,\beta}(Q,w) \tag{3}$$

where, k_f and k_i are the final and the incident wave vectors, respectively. $\gamma r_0 = 5.39$ fm is the magnetic scattering amplitude for an electron. g is the Lande factor of Co, $F(Q)$ is the isotropic form factor for Co^{2+}, and e^{-2W} is the Debye–Waller factor. $S^{\alpha,\beta}(Q,w)$ is the response function describing spin correlations.[76] The calculated spectra are convoluted by a Gaussian function with FWHM of 0.21 meV to account for the instrumental resolution, measured at room temperature with a solid vanadium rod. Error bars represent standard deviations.

In order to directly compare the calculations with the experimental INS data on the powder samples, the calculated INS cross-section (eqn (3)) was averaged over different Q vectors lying on a constant-Q sphere. The exchange constants for all samples were obtained by fitting the energy spectra at different momentum transfers (Fig. 6a). We found that for the bulk and spherical nanoparticle samples, $J_1 = -7.60$ meV, $J_2 = 1.10$ meV, and $D_S = 0.015$ meV. Using these values we were able to calculate neutron scattering spectra that compare well and reproduce all the features of the experimental data (Fig. 6b and c). However, the best fit of the energy spectra for the cubic nanoparticles was obtained with a slightly increased $J_1 = -7.72$ meV. The calculated neutron scattering spectra with these exchange parameters can reproduce the experimental data quite well (Fig. S8†). Increased value of J_1 can also explain the shift of the inelastic peak position in $I(E)$ data, experimentally observed for the cubic nanoparticles (Fig. 5c). The increase of J_1 value in the cubic nanoparticles is rather weak compared to the bulk value, presumably due to a large polydispersity of the cubic nanoparticles and their shape irregularities observed in TEM studies. Additional neutron scattering experiments on monodisperse cubic nanoparticles of various sizes might show an even larger increase of J_1 value.

The values obtained in this experiment are considerably higher than previously reported in the literature. DFT calculations with Dudraev correction for on-site Coulomb interactions (DFT+U) found the value of J_1 ranging from −0.2 to 4.8 meV for the bulk Co_3O_4, depending on the functional.[77–80] The only reported experimental value of J_1 obtained by INS measurements with a monochromatic beam on the polycrystalline Co_3O_4 powder is equal to 0.63 meV.[81]

The most likely explanation for the FM-shell in spherical nanoparticles is the reduced coordination number of the

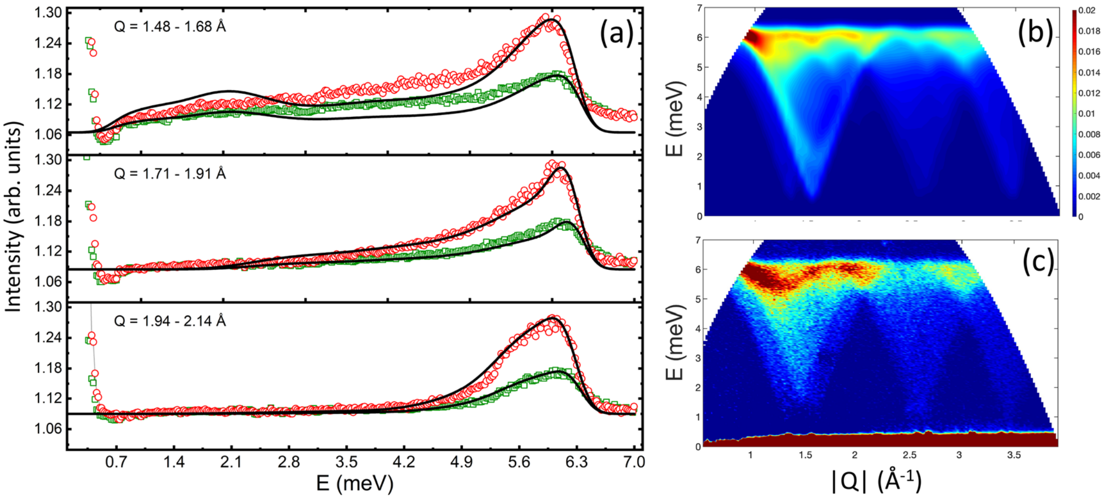

Fig. 6 (a) Energy dependence of the inelastic neutron scattering intensity at different momentum transfers Q for the bulk powder (red open circles) and the cubic nanoparticles (green open squares). The solid lines are the calculated results, as described in the text. The calculated (b) and experimental (c) $I(Q,E)$ at 5 K for the bulk Co_3O_4 powder.

surface atoms[56] or the surface spins pinning by the ligand atoms.[82–85] Both effects can induce a net magnetic moment at the surface due to incomplete AFM alignment of the magnetic moments of the surface atoms. The exchange interactions between this FM-like magnetic moment and AFM inner core lead to non-zero H_{EB}, only observed in the spherical nanoparticles. The lower coordination number of the surface atoms might lead to a defective crystal structure at the surface. Indeed, according to our neutron diffraction studies O and Co atoms deficiencies are the most prominent in the spherical nanoparticles. According to first-principle studies, oxygen vacancies lead to FM-like behavior in Co_3O_4 thin films because they affect exchange interactions between metallic ions.[86] The detailed model of the vacancies distribution in our samples is missing, but independent magnetization and Raman scattering measurements, both suggest that the vacancies are distributed at the surface of the spherical nanoparticles. Another consequence of the surface disorder in the spherical nanoparticles is the reduction of their lattice constant. The defective surface structure induces a tensile surface stress that in turn compresses the lattice constant to minimize the surface energy.[16,87,88] Our explanation is supported by the previous X-ray absorption fine structure measurements and DFT calculations on similarly sized Co_3O_4 nanostructures.[59] The cubic nanoparticles appear to be more ordered than the spherical ones, showing only small deviations in the crystal and magnetic structures from their bulk counterpart. The most prominent structural feature of the cubic nanoparticles is their surface. They are exposing well-defined crystal planes formed by high-temperature annealing in a vacuum. Previous studies have concluded that for the cubic Co_3O_4 nanoparticles, the most likely exposed planes at their surface are (111) and (100).[16] These two planes have a larger fraction of Co^{2+} ions, compared to a number of non-magnetic Co^{3+} ions. The size of Co^{2+} ions (0.745 Å) is larger than the size of Co^{3+} ions (0.545 Å), hence negative stress is induced on the surface of those planes.[66,87] That results in an increase of the lattice constant observed in our cubic sample and in previous studies of cubic Co_3O_4 nanoparticles prepared by a similar high-temperature annealing method.[61,89]

One would expect increased values of J_1 in nanoparticles with the smallest lattice constants due to a higher degree of 3d electron cloud overlap.[90] Fig. 7a shows the nearest (L_1) and the next-nearest (L_2) neighbor distances between Co^{2+} ions for all three samples obtained from neutron data refinements. The best Rietveld refinements were obtained with the position of all atoms fixed. Thus both distances follow the same dependencies as the lattice constants, *i.e.* the shortest bond lengths were found for the spherical nanoparticles. We further examine any possible local distortions of L_1 and L_2 by relaxing the positions of Co atoms in tetrahedral and octahedral sites during neutron PDF data boxcar refinements in the range r = 1.5–40 Å, with a step of r_{max} = 5 Å (Fig. 7b and c). The obtained values of L_1 and L_2 show no r_{max}-dependence and remain constants within experimental error, as well as Co–O and O–O bond lengths (Fig. S9†). We tried to relax and fit the positions of all atoms simultaneously, but it led to the over-parametrization of the model and the fits were unstable. In conclusion, we found no local distortions of the bond lengths in the superexchange path in our samples that could have explained the increased values of J_1 in the cubic nanoparticles.

Another parameter to consider when explaining the exchange interactions in a normal spinel is inversion.[86,91] Our cubic nanoparticles might be susceptible to inversion because they were exposed to high temperatures of 400 °C. We accurately calculated the inversibility parameter using the spinel anion parameter u, according to[92] for all our samples, using lattice constants and bond lengths at 10 K derived from neutron diffraction studies. The value of 0.26(1) for all three samples is consistent with the bulk values of 0.26–0.27 previously reported for a normal spinel structure.[92,93]

As we discussed in the preceding sections, the enhancement of J_1 observed in cubic nanoparticles cannot be explained by either decreased lattice constants, ligand interactions, or inversion. Thus, the shape effects must be considered. The previous reports have already indicated that the shape effects modify the magnetic structure of Co_3O_4 nanoparticles in a significant way. For example, 7 nm Co_3O_4 single-crystal nanowires showed an induced FM-moment due to the symmetry breaking of Co^{3+} ions on (111) surfaces.[52] Similarly, cubic and platelet-like Co_3O_4 nanoparticles displayed a variation in the net magnetic moment depending on the coordination number of Co ions at a dominant crystal plane.[16] In the

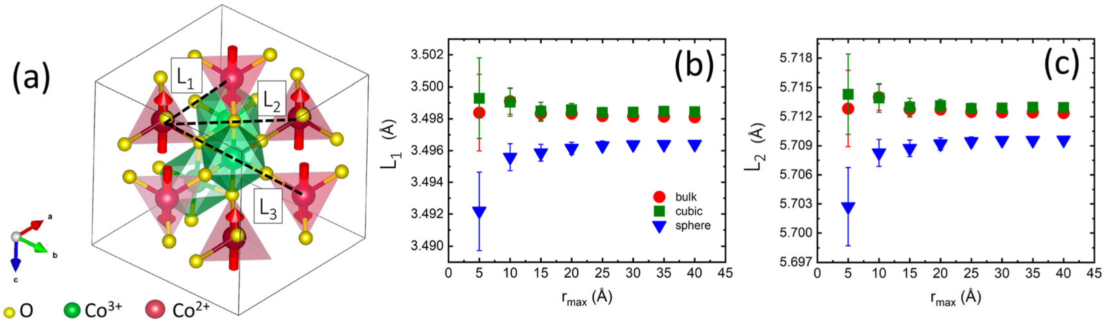

Fig. 7 (a) The nearest L_1, next-nearest neighbors L_2 and the next next-nearest neighbors L_3 distances for magnetic Co^{2+} ions in Co_3O_4. (b) L_1 and (c) L_2 obtained from the neutron PDF data refinements at 10 K, as a function of r_{max}.

case of our cubic nanoparticles, the high-resolution TEM study verified that the dominant (100) and (111) planes are exposed on the surface (Fig. 8). Presumably, exposure of these planes seen only in cubic nanoparticles is responsible for enhancing J_1. Previous studies of larger Co_3O_4 particles in the shape of cubes with the (001) plane, truncated octahedrons with (001) and (111) planes and an octahedron with the (111) show remarkably different physicochemical behaviors, as for example indicated by their respective electrochemical performances.[8] Accordingly, the key role of specifically exposed surface planes in Co_3O_4 nanoparticles with well-defined shapes must be considered. In the same vein, DFT calculations of the magnetic interactions on (100) and (111) surfaces of our cubic nanoparticles, including an experimental crystal structure can help to elucidate the origin of J_1 increase. However, given the relatively large size of the cubic nanoparticles (61 nm), those calculations are extremely time-consuming and difficult to handle. The large polydispersity of our cubic nanoparticles will further complicate the understanding of the DFT calculation results.

Finally, we considered an alternative explanation of AFM-order in our samples and a possible reason for the FM-like phase observed in the spherical Co_3O_4 nanoparticles. The idea was first put forward by W. Roth in his original work in 1964.[1] He suggested another exchange parameter J_3 between the next-next nearest neighbor of Co^{2+} ions separated by 6.68 Å and including 180° bond angle between O–Co^{3+}–O (see Fig. 7a). This is a weak interaction, but it becomes dominant if the multiplicity of exchange paths is taken into account. Each of the FM and AFM exchange paths *via* 90° O–Co^{3+}–O bonds have the same multiplicity of 24 and cancel each other out. Only the AFM exchange path *via* 180° O–Co^{3+}–O bond with a multiplicity of 12 remains responsible for AFM order in Co_3O_4. However, in Co_3O_4 nanoparticles with well-defined shapes, the multiplicity on the surface is broken and additional FM or AFM interactions are emerging.[16] We found no experimental evidence of this scenario in our samples. Using additional exchange parameter J_3 in the spin Hamiltonian had no effect on the calculated spin wave spectrum for all three samples, however, the determination of J_3 might be hindered by the powder averaged data. Additional INS measurements of a single crystal are needed for a proper assessment of the J_3 contribution to the spin wave spectrum of Co_3O_4.

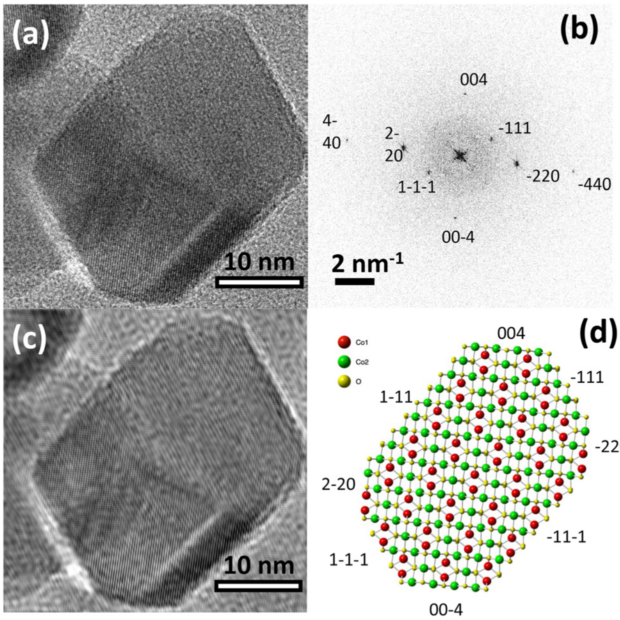

Fig. 8 Analysis of high-resolution TEM images. (a) A truncated octahedron with its corresponding indexed FFT image (b) and (c) FFT-filtered TEM image using the reflections indicated in (b) to enhance the lattice spacings. (d) Crystal structure reconstruction of the particle indicates the Miller indices of the bounding facets (not at scale).

4 Conclusions

We carried out extensive experimental studies of the structural and magnetic properties of spherical and cubic Co_3O_4 nanoparticles and compared them with the bulk powder. The spherical nanoparticles showed a pronounced effect of the canted surface spins, resulting in the appearance of an FM-like phase below 25 K. Despite, this surface disorder the exchange constants J_1 and J_2 of the spherical nanoparticles remained the same as in bulk, within the experimental error of our experiment. For the cubic nanoparticles, the lattice constant is increased as compared to the lattice constant of their bulk counterpart. It is a direct consequence of the negative surface stress caused by the high-temperature annealing. The importance of the particle's shape was further reinforced by the inelastic neutron scattering experiments, which showed increased exchange constant J_1 only for the cubic nanoparticles. Our results imply that magnetic nanoparticles with selectively exposed surface planes can strengthen the exchange interactions and hence be more attractive for magnonics applications. Those applications can also benefit from the use of the spherical Co_3O_4 nanoparticles with magnetically disordered surfaces because they still retain their bulk-like spin waves dispersion.

Author contributions

MF corresponding author, concept, measurements, data analysis, writing and editing; ZH, YX INS data analysis, writing; XT sample preparation; WL, NN, AP, MG, YS INS measurements, data reduction, editing; JCN, ME neutron PDF measurements, data reduction, editing; GSA, SU, LZ, SE HRTEM measurements, editing, data analysis, writing; MV Raman measurements, data analysis, writing; AQ SEM measurements, editing, data analysis, MCA concept, INS measurements.

Conflicts of interest

There are no conflicts to declare.

Acknowledgements

We thank Paul Hering and Dr Moo-Sung Kim for their help with laboratory X-ray diffraction measurements. We gratefully acknowledge fruitful discussions with Dr Jörg Perβon, Dr Nicolo Violini and Dr Jörg Voigt. We also thank Dr Mark Hagen for his help with CNCS measurements. We thank Dr Vaclav Petříček for modifying Jana2006 program to adopt TOF neutron diffraction data. This work is based upon experiments performed at the TOFTOF instrument operated by Technische Universität München at the Heinz Maier-Leibnitz Zentrum (MLZ), Garching, Germany. A portion of this research at Oak Ridge National Laboratory's Spallation Neutron Source was sponsored by the Scientific User Facilities Division, Office of Basic Energy Sciences, U.S. Department of Energy. This research used JEOL2100F of the Center for Functional Nanomaterials, which is a U.S. DOE Office of Science Facility, at Brookhaven National Laboratory under Contract No. DE-SC0012704. G. S. A. and S. U. thank the financial support of the Swedish Research Agency, VR (Grant No. 2016-06959) and also acknowledge Myfab Uppsala for providing facilities and experimental support. Myfab is funded by the Swedish Research Council (Grant No. 2019-00207) as a national research infrastructure.

References

1 W. Roth, *J. Phys. Chem. Solids*, 1964, **25**, 1–10.
2 D. Scheerlinck, S. Hautecler and W. Wegener, *Phys. Status Solidi B*, 1975, **68**, 535–541.
3 Y. Ichiyanagi and S. Yamada, *Polyhedron*, 2005, **24**, 2813–2816.
4 W. Söllinger, W. Heiss, R. T. Lechner, K. Rumpf, P. Granitzer, H. Krenn and G. Springholz, *Phys. Rev. B: Condens. Matter Mater. Phys.*, 2010, **81**, 155213.
5 R. Zhang, L. Pan, B. Guo, Z.-F. Huang, Z. Chen, L. Wang, X. Zhang, Z. Guo, W. Xu, K. P. Loh and J.-J. Zou, *J. Am. Chem. Soc.*, 2023, **145**, 2271–2281.
6 M. A. Boles, D. Ling, T. Hyeon and D. V. Talapin, *Nat. Mater.*, 2016, **15**, 141–153.
7 X. Xie, Y. Li, Z.-Q. Liu, M. Haruta and W. Shen, *Nature*, 2009, **458**, 746–749.
8 X. Xiao, X. Liu, H. Zhao, D. Chen, F. Liu, J. Xiang, Z. Hu and Y. Li, *Adv. Mater.*, 2012, **24**, 5762–5766.
9 C. Gao, Q. Meng, K. Zhao, H. Yin, D. Wang, J. Guo, S. Zhao, L. Chang, M. He, Q. Li, H. Zhao, X. Huang, Y. Gao and Z. Tang, *Adv. Mater.*, 2016, **28**, 6485–6490.
10 J. Mu, L. Zhang, G. Zhao and Y. Wang, *Phys. Chem. Chem. Phys.*, 2014, **16**, 15709–15716.
11 T. He, D. Chen, X. Jiao and Y. Wang, *Adv. Mater.*, 2006, **18**, 1078–1082.
12 D. Su, X. Xie, P. Munroe, S. Dou and G. Wang, *Sci. Rep.*, 2014, **4**, 6519.
13 R. Jing, A. Shan, R. Wang and C. Chen, *CrystEngComm*, 2013, **15**, 3587–3592.
14 Y. Hou, H. Kondoh, M. Shimojo, T. Kogure and T. Ohta, *J. Phys. Chem. B*, 2005, **109**, 19094–19098.
15 Y. Wang, Y. Lei, J. Li, L. Gu, H. Yuan and D. Xiao, *ACS Appl. Mater. Interfaces*, 2014, **6**, 6739–6747.
16 M. Shepit, V. K. Paidi, C. A. Roberts and J. van Lierop, *Sci. Rep.*, 2020, **10**, 20990.
17 S. Takada, M. Fujii, S. Kohiki, T. Babasaki, H. Deguchi, M. Mitome and M. Oku, *Nano Lett.*, 2001, **1**, 379–382.
18 I. Lorite, J. J. Romero and J. F. Fernández, *J. Raman Spectrosc.*, 2012, **43**, 1443–1448.
19 Y. Liu, H. Wan, H. Zhang, J. Chen, F. Fang, N. Jiang, W. Zhang, F. Zhou, H. Arandiyan, Y. Wang, G. Liu, Z. Wang, S. Luo, X. Chen and H. Sun, *ACS Appl. Nano Mater.*, 2020, **3**, 3892–3903.
20 H. Qin, R. B. Holländer, L. Flajšman, F. Hermann, R. Dreyer, G. Woltersdorf and S. van Dijken, *Nat. Commun.*, 2021, **12**, 2293.
21 S. Neusser and D. Grundler, *Adv. Mater.*, 2009, **21**, 2927–2932.
22 A. Kamra and L. G. Johnsen, *Nat. Phys.*, 2023, **19**, 469–470.
23 V. Sluka, T. Schneider, R. A. Gallardo, A. Kákay, M. Weigand, T. Warnatz, R. Mattheis, A. Roldán-Molina, P. Landeros, V. Tiberkevich, A. Slavin, G. Schütz, A. Erbe, A. Deac, J. Lindner, J. Raabe, J. Fassbender and S. Wintz, *Nat. Nanotechnol.*, 2019, **14**, 328–333.
24 R. Salikhov, I. Ilyakov, L. Körber, A. Kákay, R. A. Gallardo, A. Ponomaryov, J.-C. Deinert, T. V. A. G. de Oliveira, K. Lenz, J. Fassbender, S. Bonetti, O. Hellwig, J. Lindner and S. Kovalev, *Nat. Phys.*, 2023, **19**, 529–535.
25 J. Pelliciari, S. Lee, K. Gilmore, J. Li, Y. Gu, A. Barbour, I. Jarrige, C. H. Ahn, F. J. Walker and V. Bisogni, *Nat. Mater.*, 2021, **20**, 188–193.
26 D. Lachance-Quirion, S. P. Wolski, Y. Tabuchi, S. Kono, K. Usami and Y. Nakamura, *Science*, 2020, **367**, 425–428.
27 O. Gomonay, T. Jungwirth and J. Sinova, *Phys. Status Solidi RRL*, 2017, **11**, 1700022.
28 E. Albisetti, S. Tacchi, R. Silvani, G. Scaramuzzi, S. Finizio, S. Wintz, C. Rinaldi, M. Cantoni, J. Raabe, G. Carlotti, R. Bertacco, E. Riedo and D. Petti, *Adv. Mater.*, 2020, **32**, 1906439.
29 M. Ishibashi, Y. Shiota, T. Li, S. Funada, T. Moriyama and T. Ono, *Sci. Adv.*, 2020, **6**, eaaz6931.
30 Z. Cai, Y. Bi, E. Hu, W. Liu, N. Dwarica, Y. Tian, X. Li, Y. Kuang, Y. Li, X.-Q. Yang, H. Wang and X. Sun, *Adv. Energy Mater.*, 2018, **8**, 1701694.
31 W. Li, Y. Wang, X. Y. Cui, S. Yu, Y. Li, Y. Hu, M. Zhu, R. Zheng and S. P. Ringer, *ACS Appl. Mater. Interfaces*, 2018, **10**, 19235–19247.
32 E. M. Jefremovas, M. de la Fuente Rodríguez, F. Damay, B. Fåk, A. Michels, J. A. Blanco and L. F. Barquín, *Phys. Rev. B*, 2021, **104**, 134404.
33 E. M. Jefremovas, M. de la Fuente Rodríguez, D. Alba Venero, C. Echevarría-Bonet, P. Bender, B. Fåk, J. A. Blanco and L. Fernández Barquín, *Commun. Mater.*, 2023, **4**, 56.
34 M. Feygenson, X. Teng, S. E. Inderhees, Y. Yiu, W. Du, W. Han, J. Wen, Z. Xu, A. A. Podlesnyak, J. L. Niedziela,

M. Hagen, Y. Qiu, C. M. Brown, L. Zhang and M. C. Aronson, *Phys. Rev. B: Condens. Matter Mater. Phys.*, 2011, **83**, 174414.

35 O. M. Sousa, J. S. Lima, A. F. Lima and M. V. Lalic, *J. Magn. Magn. Mater.*, 2019, **484**, 21–30.

36 A. Lima, *J. Phys. Chem. Solids*, 2016, **91**, 86–89.

37 V. P. Puntes, K. M. Krishnan and P. A. Alivisatos, *Science*, 2001, **291**, 2115–2117.

38 M. Feygenson, Y. Yiu, A. Kou, K.-S. Kim and M. C. Aronson, *Phys. Rev. B: Condens. Matter Mater. Phys.*, 2010, **81**, 195445.

39 J. Neuefeind, M. Feygenson, J. Carruth, R. Hoffmann and K. K. Chipley, *Nucl. Instrum. Methods Phys. Res., Sect. B*, 2012, **287**, 68–75.

40 V. Petříček, M. Dušek and L. Palatinus, *Z. Kristallogr. – Cryst. Mater.*, 2014, **229**, 345–352.

41 G. Ehlers, A. A. Podlesnyak, J. L. Niedziela, E. B. Iverson and P. E. Sokol, *Rev. Sci. Instrum.*, 2011, **82**, 085108.

42 O. Arnold, J. Bilheux, J. Borreguero, A. Buts, S. Campbell, L. Chapon, M. Doucet, N. Draper, R. F. Leal, M. Gigg, V. Lynch, A. Markvardsen, D. Mikkelson, R. Mikkelson, R. Miller, K. Palmen, P. Parker, G. Passos, T. Perring, P. Peterson, S. Ren, M. Reuter, A. Savici, J. Taylor, R. Taylor, R. Tolchenov, W. Zhou and J. Zikovsky, *Nucl. Instrum. Methods Phys. Res., Sect. A*, 2014, **764**, 156–166.

43 Y. Ikedo, J. Sugiyama, H. Nozaki, H. Itahara, J. Brewer, E. Ansaldo, G. Morris, D. Andreica and A. Amato, *Phys. Rev. B: Condens. Matter Mater. Phys.*, 2007, **75**, 054424.

44 T. Fukai, Y. Furukawa, S. Wada and K. Miyatani, *J. Phys. Soc. Jpn.*, 1996, **65**, 4067–4071.

45 P. Sahoo, H. Djieutedjeu and P. F. P. Poudeu, *J. Mater. Chem. A*, 2013, **1**, 15022–15030.

46 A. H. Hill, A. Harrison, C. Ritter, W. Yue and W. Zhou, *J. Magn. Magn. Mater.*, 2011, **323**, 226–231.

47 L. He, C. Chen, N. Wang, W. Zhou and L. Guo, *J. Appl. Phys.*, 2007, **102**, 103911.

48 D. von Dreifus, E. C. Pereira and A. J. A. de Oliveira, *Mater. Res. Express*, 2015, **2**, 116102.

49 D. Branković, V. Jokanović, B. Babić-Stojić, Z. Jagličić, D. Lisjak and D. Kojić, *J. Phys.: Condens. Matter*, 2009, **21**, 095303.

50 S. Sarkar, A. Mondal, N. Giri and R. Ray, *Phys. Chem. Chem. Phys.*, 2019, **21**, 260–267.

51 M. Kofu, R. Watanuki, T. Sakakibara, S. Ohira-Kawamura, K. Nakajima, M. Matsuura, T. Ueki, K. Akutsu and O. Yamamuro, *Sci. Rep.*, 2021, **11**, 12098.

52 P. Lv, Y. Zhang, R. Xu, J. C. Nie and L. He, *J. Appl. Phys.*, 2012, **111**, 013910.

53 E. L. Salabaş, A. Rumplecker, F. Kleitz, F. Radu and F. Schuth, *Nano Lett.*, 2006, **6**, 2977–2981.

54 Z. Dong, Y. Fu, Q. Han, Y. Xu and H. Zhang, *J. Phys. Chem. C*, 2007, **111**, 18475–18478.

55 S. D. Li, H. Bi, J. L. Fang, W. Zhong and Y. W. Du, *Chin. Phys. Lett.*, 2004, **21**, 737–740.

56 P. Dutta, M. S. Seehra, S. Thota and J. Kumar, *J. Phys.: Condens.Matter*, 2008, **20**, 015218.

57 M. J. Benitez, O. Petracic, H. Tüysüz, F. Schüth and H. Zabel, *Europhys. Lett.*, 2009, **88**, 1–6.

58 V. G. Hadjiev, M. N. Iliev and I. V. Vergilov, *J. Phys. C: Solid State Phys.*, 1988, **21**, L199.

59 R. Zhang, Y.-C. Zhang, L. Pan, G.-Q. Shen, N. Mahmood, Y.-H. Ma, Y. Shi, W. Jia, L. Wang, X. Zhang, W. Xu and J.-J. Zou, *ACS Catal.*, 2018, **8**, 3803–3811.

60 H. Shirai, Y. Morioka and I. Nakagawa, *J. Phys. Soc. Jpn.*, 1982, **51**, 592–597.

61 S. R. Gawali, A. C. Gandhi, S. S. Gaikwad, J. Pant, T.-S. Chan, C.-L. Cheng, Y.-R. Ma and S. Y. Wu, *Sci. Rep.*, 2018, **8**, 249.

62 L. C. Schumacher, I. B. Holzhueter, I. R. Hill and M. J. Dignam, *Electrochim. Acta*, 1990, **35**, 975–984.

63 C. Stella, N. Soundararajan and K. Ramachandran, *AIP Adv.*, 2015, **5**, 087104.

64 G. Gouadec and P. Colomban, *Prog. Cryst. Growth Charact. Mater.*, 2007, **53**, 1–56.

65 D. Gallant, M. Pézolet and S. Simard, *J. Phys. Chem. B*, 2006, **110**, 6871–6880.

66 P. Meena, R. Kumar and K. Sreenivas, *AIP Conf. Proc.*, 2013, 1204–1205.

67 T. D. Sparks, A. Gurlo, M. F. Bekheet, M. W. Gaultois, G. Cherkashinin, L. Laversenne and D. R. Clarke, *Phys. Rev. B*, 2019, **99**, 1–10.

68 N. Golosova, D. Kozlenko, D. Nicheva, T. Petkova, S. Kichanov, E. Lukin, G. Avdeev, P. Petkov and B. Savenko, *J. Magn. Magn. Mater.*, 2020, **508**, 166874.

69 S. Thota, A. Kumar and J. Kumar, *J. Mater. Sci. Eng. B*, 2009, **164**, 30–37.

70 D. A. Resnick, K. Gilmore, Y. U. Idzerda, M. T. Klem, M. Allen, T. Douglas, E. Arenholz and M. Young, *J. Appl. Phys.*, 2006, **99**, 08Q501.

71 K. M. Jensen and S. R. Cooper, *Reference Module in Chemistry, Molecular Sciences and Chemical Engineering*, Elsevier, 2021.

72 T. Köhler, A. Feoktystov, O. Petracic, N. Nandakumaran, A. Cervellino and T. Brückel, *J. Appl. Crystallogr.*, 2021, **54**, 1719–1729.

73 A. Lappas, G. Antonaropoulos, K. Brintakis, M. Vasilakaki, K. N. Trohidou, V. Iannotti, G. Ausanio, A. Kostopoulou, M. Abeykoon, I. K. Robinson and E. S. Bozin, *Phys. Rev. X*, 2019, **9**, 041044.

74 H. L. Andersen, B. A. Frandsen, H. P. Gunnlaugsson, M. R. V. Jørgensen, S. J. L. Billinge, K. M. Ø. Jensen and M. Christensen, *IUCrJ*, 2021, **8**, 33–45.

75 Private communications with Dr. Jörg Perβon, 2020.

76 *Theory of neutron scattering from condensed matter. Vol. 1. Nuclear scattering*.

77 A. Cadi-Essadek, A. Roldan, D. Santos-Carballal, P. E. Ngoepe, M. Claeys and N. H. de Leeuw, *S. Afr. J. Chem.*, 2021, **74**, 8–16.

78 J. Chen, X. Wu and A. Selloni, *Phys. Rev. B: Condens. Matter Mater. Phys.*, 2011, **83**, 1–7.

79 V. Singh, M. Kosa, K. Majhi and D. T. Major, *J. Chem. Theory Comput.*, 2015, **11**, 64–72.

80 P. Gopal, R. D. Gennaro, M. S. dos Santos Gusmao, R. A. R. A. Orabi, H. Wang, S. Curtarolo, M. Fornari and M. B. Nardelli, *J. Phys.: Condens. Matter*, 2017, **29**, 444003.

81 D. Scheerlinck and S. Hautecler, *Phys. Status Solidi B*, 1976, **73**, 223–228.

82 R. H. Kodama, A. E. Berkowitz, E. McNiff Jr. and S. Foner, *Phys. Rev. Lett.*, 1996, **77**, 394.

83 A. Berkowitz, J. Lahut, I. Jacobs, L. M. Levinson and D. Forester, *Phys. Rev. Lett.*, 1975, **34**, 594.

84 D. Lin, A. Nunes, C. Majkrzak and A. Berkowitz, *J. Magn. Magn. Mater.*, 1995, **145**, 343–348.

85 L. Shan-Dong, B. Hong, F. Jiang-Lin, Z. Wei and D. You-Wei, *Chin. Phys. Lett.*, 2004, **21**, 737.

86 P. Wang, C. Jin, P. Li, D. X. Zheng, J. L. Gong and H. L. Bai, *Thin Solid Films*, 2018, **660**, 287–293.

87 P. M. Diehm, P. Ágoston and K. Albe, *ChemPhysChem*, 2012, **13**, 2443–2454.

88 M. Casas-Cabanas, G. Binotto, D. Larcher, A. Lecup, V. Giordani and J. M. Tarascon, *Chem. Mater.*, 2009, **21**, 1939–1947.

89 P. P. Rodenbough, C. Zheng, Y. Liu, C. Hui, Y. Xia, Z. Ran, Y. Hu, S. W. Chan and W. Wong-Ng, *J. Am. Ceram. Soc.*, 2017, **100**, 384–392.

90 H. Ueda and Y. Ueda, *Phys. Rev. B: Condens. Matter Mater. Phys.*, 2008, **77**, 224411.

91 W. Chen, C. Chen and L. Guo, *J. Appl. Phys.*, 2010, **108**, 073907.

92 R. J. Hill, J. R. Craig and G. V. Gibbs, *Phys. Chem. Miner.*, 1979, **4**, 317–339.

93 K. E. Sickafus, J. M. Wills and N. W. Grimes, *J. Am. Ceram. Soc.*, 1999, **82**, 3279–3292.